

A robust fourth-order finite-difference discretization for the strongly anisotropic transport equation in magnetized plasmas

L. Chacón^{a,*}, Jason Hamilton^a, Natalia Krasheninnikova^a

^a*Los Alamos National Laboratory, Los Alamos, NM 87545, USA*

Abstract

We propose a second-order temporally implicit, fourth-order-accurate spatial discretization scheme for the strongly anisotropic heat transport equation characteristic of hot, fusion-grade plasmas. Following [Du Toit et al., *Comp. Phys. Comm.*, **228** (2018)], the scheme transforms mixed-derivative diffusion fluxes (which are responsible for the lack of a discrete maximum principle) into nonlinear advective fluxes, amenable to nonlinear-solver-friendly monotonicity-preserving limiters. The scheme enables accurate multi-dimensional heat transport simulations with up to seven orders of magnitude of heat-transport-coefficient anisotropies with low cross-field numerical error pollution and excellent algorithmic performance, with the number of linear iterations scaling very weakly with grid resolution and grid anisotropy, and scaling with the square-root of the implicit timestep. We propose a multigrid preconditioning strategy based on a second-order-accurate approximation that renders the scheme efficient and scalable under grid refinement. Several numerical tests are presented that display the expected spatial convergence rates and strong algorithmic performance, including fully nonlinear magnetohydrodynamics simulations of kink instabilities in a Bennett pinch in 2D helical geometry and of ITER in 3D toroidal geometry.

Keywords: anisotropic transport, implicit methods, magnetized plasmas, multigrid, fourth-order-accurate finite differences

PACS:

1. Introduction

This study is concerned with the solution of the strongly anisotropic transport equation in magnetized plasmas. Plasmas in tokamak (and similar fusion devices) rely on a dominant axial field that limits cross-field transport, which would otherwise degrade the confinement by allowing energy to escape to the walls. Theoretical estimates, experimental measurements, and modeling suggest that the transport anisotropy in common tokamak reactors can reach extremely high values $\chi_{\parallel}/\chi_{\perp} \sim 10^7 - 10^{10}$ [1, 2, 3, 4, 5, 6], making solving this equation a formidable numerical challenge. Such strong magnetization leads to much higher transport anisotropy than that found in other applications, and thus presents unique numerical challenges for simulating realistic plasma conditions in simulations.

*Corresponding author

Email address: chacon@lanl.gov (L. Chacón)

The numerical challenges are present both spatially and temporally. Spatially, strongly anisotropic diffusion equations suffer from numerical pollution of the perpendicular dynamics from the large parallel transport term [7], and the lack of a maximum principle (which may lead to negative temperatures). Numerical pollution can be mitigated by the use of high-order spatial discretizations [8, 9] and/or so-called “symmetric” discretizations [10, 9, 11, 12], but these lack a maximum principle. The maximum principle can be enforced via nonlinear limiters [13, 14, 15, 16, 17] or via locally identifying diffusion directions [18, 19, 20], but the former typically result in low-order spatial discretizations (and, depending on the limiter used, strong nonlinearity), and the latter lose local conservation, of critical importance in many applications of interest. Temporally, explicit methods are constrained to very small time steps due to the Courant stability condition, determined by the largest diffusion coefficient (i.e., the parallel transport one). For implicit methods, the issue is the near-degeneracy of the associated algebraic systems due to the strong transport anisotropy [21], and the ill-conditioning of associated algebraic systems that makes them difficult to invert using modern, efficient iterative methods. Most of the previous studies using implicit methods resorted to direct solvers for the temporal update, with some authors resorting to implicit/explicit integrators to ameliorate the size of the resulting matrices on a per-parallel-task basis [22]. More recent studies [23] have explored approximate-block-factorization preconditioners for GMRES for the micro-macro formulation of Ref. [24], demonstrating significant potential for controlling the number of GMRES iterations but so far only for mesh-aligned and simply connected magnetic-field topologies (i.e, without islands).

Recently, a series of studies have proposed asymptotic-preserving (AP) schemes for the anisotropic transport equation [25, 26, 24, 27, 28] with the property that the numerical error and matrix conditioning do not scale with the anisotropy ratio $\chi_{\parallel}/\chi_{\perp}$. Refs. [25, 26, 24] considered only open field lines in a time-independent context. In contrast, Ref. [28] considered only closed ones, also in a time-independent context. Ref. [27] considered the time-dependent case for open and closed magnetic fields with implicit timestepping. However, it is unclear how the approach can generalize to three dimensions (where confined stochastic field lines of infinite length may exist), and the reference employed a direct linear solver, which is known to scale very poorly with mesh refinement and with processor count in parallel environments.

A separate AP line of research is a semi-Lagrangian scheme based on a Green’s function formulation of the heat transport equation, where parallel fast transport is resolved essentially semi-analytically [29, 30, 21, 31, 32]. Those methods ensure the absence of pollution due to their asymptotic preserving nature [21] in the limit of infinite anisotropy [29, 30], can deal with nonlocal heat closures [21] and arbitrary magnetic field topology [31], and allow for implicit timestepping [32]. However, to date, these methods need to be demonstrated with nonlinear transport coefficients, have not been extended to deal with general boundary conditions for the magnetic field, and have not yet been coupled with richer physics models such as magnetohydrodynamics (MHD).

This study proposes a practical implicit Eulerian spatio-temporal discretization for the strongly anisotropic transport equation which, while not AP, features several desirable properties, including:

- Manageable numerical pollution for reasonable anisotropies, demonstrated here up to

$\chi_{\parallel}/\chi_{\perp} \sim 10^7$ (which in 2D correspond to $\sim 10^9$ anisotropies in 3D for large-magnetic-guide field configurations such as tokamaks [22]).

- Numerical robustness against developing negative temperatures for fourth-order accurate discretizations, and strict positivity for second-order ones.
- Strict local conservation properties.
- Suitability for modern nonlinear solvers (e.g., Jacobian-free Newton-Krylov – JFNK [33]) with efficient multigrid preconditioning for scalability.
- Compatibility and ease of implementation in existing finite-difference multiphysics simulation codes (e.g., MHD).

Our implementation employs nonlinear flux limiters following the key insight proposed in Ref. [17] (in the context of the Fokker-Planck collision operator). The reference proposed to reformulate mixed-derivative terms in the diffusion operator as nonlinear advection operators, to which positivity-preserving limiters that are compatible with nonlinear iterative solvers can be applied (here we use a variant of the SMART advective scheme [34]). Our contributions beyond that study include:

- Extension to fourth-order accuracy (critical for dealing with strong anisotropies, as we shall see).
- Development of effective and scalable multigrid preconditioning strategies that render the linear and nonlinear iteration count manageable for sufficiently large timesteps (measured as $\Delta t \chi_{\parallel}$).
- Demonstration on challenging anisotropic transport problems, including full 3D MHD simulations of fusion-grade plasmas.

The rest of this paper is organized as follows. The model of interest along with spatial and temporal discretization details is introduced in Sec. 2. Section 3 demonstrates the properties of the scheme with several challenging numerical tests, including fully featured MHD simulations of kink instabilities in a Bennett pinch [35] in 2D, and in the ITER fusion reactor in 3D. We finally conclude with Sec. 4.

2. Model equations, numerical discretization, and solver strategy

The anisotropic heat transport equation in magnetized plasmas reads:

$$\partial_t T - \nabla \cdot (\bar{\Xi}(T) \cdot \nabla T) \equiv S, \quad (1)$$

where $T = T(t, \mathbf{x})$ is the temperature field, $S = S(t, \mathbf{x})$ is a heat source, and the tensor diffusion $\bar{\Xi}(T)$ is given by:

$$\bar{\Xi}(T) = \chi_{\parallel}(T) \mathbf{b}\mathbf{b} + \chi_{\perp}(T)(\mathbb{I} - \mathbf{b}\mathbf{b}),$$

with $\mathbf{b} = \mathbf{B}/B$ the unit vector along the magnetic field direction. The expression for the parallel and perpendicular transport coefficients for collisional fully ionized plasmas can be

found in Ref. [1], and will be discussed later in this study. The extreme transport anisotropy, $\chi_{\parallel}/\chi_{\perp} \sim 10^7 - 10^{10}$, makes finding the solution of this equation a formidable numerical challenge (as advanced in the previous section).

In this study, we propose an accessible higher-order finite-difference spatial discretization with remarkable robustness and solver performance in an implicit timestepping context. Key to the approach is the reformulation of mixed-derivative terms as nonlinear advection operators [17]. In what follows, we introduce the main ingredients of the nonlinear spatial discretization and its nonlinear iterative inversion, including its linearized treatment to make the approach amenable to multigrid preconditioning.

2.1. Fourth-order discretization of the anisotropic diffusion equation

In this section we will develop a conservative, fourth-order discretization framework for the $\nabla \cdot (\bar{\Xi} \cdot \nabla T)$ operator. This discretization has been used in various earlier studies [21, 32, 31], but has never been documented in detail and we do so here. We will derive the formulas in detail for the 2D Cartesian uniform-mesh case, noting that the extension to 3D is straightforward. We also note that the extension to curvilinear geometry is also straightforward when realizing that, in curvilinear representation $\mathbf{x}(\xi)$:

$$\nabla \cdot (\bar{\Xi} \cdot \nabla) = \frac{1}{J} \partial_i (J \Xi^{ij} \partial_j),$$

with J the Jacobian of the transformation, $\partial_i = \partial/\partial \xi_i$, and $\Xi^{ij} = \nabla \xi_i \cdot \bar{\Xi} \cdot \nabla \xi_j$ the contravariant components of the tensor $\bar{\Xi}$. Therefore, the discrete treatment discussed below in Cartesian geometry can be generalized readily by considering the curvilinear tensor components $J \Xi^{ij}$ instead of the Cartesian ones, and dividing the discretization formulas by the cell Jacobian.

Our starting point is a centered, conservative discretization of the flux derivatives along a given coordinate direction, e.g.:

$$\frac{\partial F_x}{\partial x}|_{i,j} = \frac{\tilde{F}_{x,i+1/2,j} - \tilde{F}_{x,i-1/2,j}}{\Delta x}, \quad (2)$$

where $\tilde{F}_{x,i+1/2,j}$ and $\tilde{F}_{x,i-1/2,j}$ are fluxes through $(i + \frac{1}{2}, j)$ and $(i - \frac{1}{2}, j)$ faces along the x -direction, which bound the cell (i, j) . The definitions of the fluxes will determine the derivative's precision as well as other aspects, such as positivity preservation. A fourth-order centered discretization can be constructed from Eq. 2 by interpolating the fluxes using four discrete points, two at each side of the face, as:

$$\tilde{F}_{x,i+1/2,j} = \sum_{l=-1}^2 a_l F_{x,i+l,j}, \quad (3)$$

with $a_{-1} = a_2 = -\frac{1}{12}$, $a_0 = a_1 = \frac{7}{12}$.

However, the flux itself in the operator of interest is given by $F_x = \Xi^{xx} \partial_x T + \Xi^{xy} \partial_y T$,

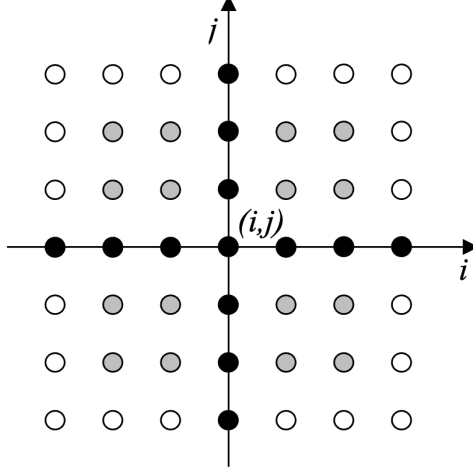


Figure 1: Combined stencil for discretization of parallel transport operator. Black points correspond to co-derivative fluxes, and gray points to cross-derivative ones.

which must be estimated to fourth-order as well. According to Eq. 3, we can write:

$$\frac{\partial}{\partial x} \left(\Xi^{xx} \frac{\partial f}{\partial x} \right) |_{i,j} = \frac{1}{\Delta x} \sum_{l=-1}^2 a_l \left(\Xi_{i+l,j}^{xx} \frac{\partial f}{\partial x} |_{i+l,j} - \Xi_{i-1+l,j}^{xx} \frac{\partial f}{\partial x} |_{i-1+l,j} \right), \quad (4)$$

$$\frac{\partial}{\partial x} \left(\Xi^{xy} \frac{\partial f}{\partial y} \right) |_{i,j} = \frac{1}{\Delta x} \sum_{l=-1}^2 a_l \left(\Xi_{i+l,j}^{xy} \frac{\partial f}{\partial y} |_{i+l,j} - \Xi_{i-1+l,j}^{xy} \frac{\partial f}{\partial y} |_{i-1+l,j} \right). \quad (5)$$

The derivatives $\frac{\partial f}{\partial x}$ and $\frac{\partial f}{\partial y}$ must be computed with at least fourth-order accuracy. Co-derivative fluxes (that is, those with both derivatives along the same direction) are calculated using a 7-point stencil. Cross-derivative fluxes are computed using a 5×5 -point stencil to fit a fourth-order polynomial. Special treatment is required at physical boundaries to retain fourth-order accuracy with a single ghost-cell layer. At logical boundaries between parallel domains, we employ the same treatment as at physical boundaries and then perform a synchronization step to average fluxes from left and right domains to enforce strict conservation. This preserves conservation and high-order accuracy without needing to communicate more than once ghost-cell layer. The resulting 29-point 2D stencil for the calculations of Eqs. 4 and 5 is illustrated in Fig. 1, and discussed in detail in Appendix A.

2.2. Reformulation and discretization of cross-derivative diffusion fluxes

Cross-diffusion fluxes are problematic from a discretization and solver robustness standpoint. At the discretization level, assuming a second-order accurate discretization for the sake of argument, cross-derivative fluxes are responsible for the lack of a maximum principle [36, 17]. Co-derivative ones are positivity-preserving for the standard second-order star-stencil, but this property is in principle lost with a fourth-order implementation. Nevertheless, we have found the scheme to be robust against developing negative temperature values in our numerical tests.

Several authors [36, 17, 16, 37] have explored the use of advective-like limiters for the cross-diffusion terms to control positivity. Here, we follow Ref. [17] because of its generality,

ease of implementation in 2D and 3D by reusing existing advective routines, and amenability to multigrid preconditioning. For exposition purposes, we consider the cross-diffusion term $\partial_x(\Xi^{xy}\partial_y T)$. In the reference, Du Toit and collaborators propose to reformulate this term as:

$$\partial_x(\Xi^{xy}\partial_y T) = \partial_x \left(T \Xi^{xy} \frac{\partial_y T}{T} \right) = \partial_x (T v_x^*(T)),$$

where $v_x^*(T) = \Xi^{xy}(\partial_y T)/T$ is a fictitious velocity. The resulting advection operator is nonlinear in T even if the original cross-diffusion term is linear, but this is to be expected as we are effectively introducing a nonlinear limiter to the cross-diffusion term to enforce positivity. In practice, the fictitious velocity can be found discretely at the face $i + 1/2$ from the cross fluxes as (from Eq. 5):

$$v_{x,i+1/2,j}^* = \frac{1}{T_{i+1/2,j}} \sum_{l=-1}^2 a_l \left(\Xi_{i+l,j}^{xy} \frac{\partial f}{\partial y} \Big|_{i+l,j} \right),$$

where the flux inside the sum is computed as detailed in Appendix A, and we estimate the face-centered temperature in the denominator by a simple average of adjacent cell centers and adding a small failsafe $\epsilon_{fs} = 10^{-4}$ to prevent it from getting too close to zero, i.e., $T_{i+1/2,j} = (T_{i,j} + T_{i+1,j})/2 + \epsilon_{fs}$.

Once so transformed, any monotonicity-preserving advective discretization scheme can in principle be used. However, most such schemes are designed for explicit integrators, which are not suitable for our application due to the numerical stiffness present from the large parallel-transport coefficients. In an implicit context, one needs to be careful as many advective limiters are highly nonlinear and not differentiable, which is problematic for the Jacobian computation in Newton's method, and therefore difficult to deal with in a nonlinear iterative solver context. In this study, we use the QUICK/second-order-upwind variant of the SMART scheme [34] for our advective discretization needs, which is up to third-order accurate when possible, and reverts locally to second- or first-order upwinding when needed to preserve monotonicity. We have found the SMART variant to be robust, well behaved, and amenable for JFNK nonlinear iterative solvers. We discuss our implicit timestepping and nonlinear solver strategy next.

2.3. Temporal discretization, nonlinear solver strategy, and multigrid preconditioning

For time discretization, we employ a second-order-accurate Backward Differentiation scheme (BDF2) [38]. BDF2 is not strictly positivity-preserving, but it provides a good balance between accuracy and robustness in practice (as our numerical tests will demonstrate).

As discussed earlier, the discretization of advective cross-fluxes is nonlinear. Additional sources of nonlinearity may originate from the transport coefficients, which may depend explicitly on the dependent variable (see e.g. [1] for fusion plasmas). This, combined with the need of implicit timestepping, implies a nonlinear solver is needed. Here we consider JFNK [33] owing to its versatility and robustness in practice.

JFNK needs to be preconditioned for efficiency (details below). In JFNK, the preconditioning step is naturally incorporated in the Krylov method (flexible GMRES [39]). Nonlinear

convergence is controlled in our implementation by the usual criterion:

$$\|\mathbf{F}(\mathbf{x}_k)\|_2 < \epsilon_a + \epsilon_r \|\mathbf{F}(\mathbf{x}_0)\|_2 = \epsilon_t, \quad (6)$$

where $\|\cdot\|_2$ is the L_2 -norm (Euclidean norm), $\epsilon_a = \sqrt{N} \times 10^{-15}$ (with N the total number of degrees of freedom) is an absolute tolerance to avoid converging below round-off, ϵ_r is the Newton relative convergence tolerance, and $\mathbf{F}(\mathbf{x}_0)$ is the initial residual. We also have the option to control convergence by directly measuring the absolute size of the Newton update:

$$\|\delta\mathbf{x}_k\| < \epsilon_s. \quad (7)$$

By default, we set $\epsilon_s = 0$ unless otherwise stated. We employ an inexact Newton method [40] in which the FGMRES convergence tolerance is adjusted every Newton iteration as follows:

$$\|J_k \delta\mathbf{x}_k + \mathbf{F}(\mathbf{x}_k)\|_2 < \zeta_k \|\mathbf{F}(\mathbf{x}_k)\|_2, \quad (8)$$

where ζ_k is the inexact Newton parameter and $J_k = \left. \frac{\partial \mathbf{F}}{\partial \mathbf{x}} \right|_k$ is the Jacobian matrix. Here, we employ the same prescription for ζ_k as in earlier studies [41, 42]:

$$\begin{aligned} \zeta_k^A &= \gamma \left(\frac{\|\mathbf{F}(\mathbf{x}_k)\|_2}{\|\mathbf{F}(\mathbf{x}_{k-1})\|_2} \right)^\alpha, \\ \zeta_k^B &= \min[\zeta_{max}, \max(\zeta_k^A, \gamma \zeta_{k-1}^\alpha)], \\ \zeta_k &= \min[\zeta_{max}, \max(\zeta_k^B, \gamma \frac{\epsilon_t}{\|\mathbf{F}(\mathbf{x}_k)\|_2})], \end{aligned}$$

with $\alpha = 1.5$, $\gamma = 0.9$, and $\zeta_{max} = 0.8$. The convergence tolerance ϵ_t is the same as in Eq. 6.

For preconditioning, we employ a geometric MG solver. The MG preconditioner inverts a low-order discretization of the heat transport equation (i.e., second-order discretization of co-derivative fluxes and first-order upwind discretization of advective ones, both linear), which is guaranteed to be h -elliptic and therefore to have the smoothing property (and to lead to a successful MG method) [43]. The nonlinear dependence on temperature in the transport coefficients (when present) and advective cross-fluxes is Picard-linearized in the MG solve to the previous nonlinear iteration. Our MG implementation features a matrix-light implementation [41, 42, 44], in which only the diagonal of the system of interest is stored for smoothing purposes. Coarse operators are found via rediscritization, and required residuals in the MG iteration are found in a matrix-free manner. For smoothing, unless otherwise specified we employ five passes of damped Jacobi (p. 10 in [45]; p. 118 in [46]), with weight $\omega = 0.7$, for both the restriction and the prolongation steps. MG restriction employs conservative agglomeration, and prolongation employs a first-order interpolation. The coarsest-mesh problem (on an 8×8 mesh) is solved with GMRES. In MG jargon, such V-cycle is identified as V(5,5), where the two integers indicate restriction and prolongation smoothing steps, respectively.

3. Numerical tests

We present several numerical tests that will demonstrate the convergence and performance properties of the fourth-order Eulerian anisotropic transport implicit algorithm. The

tests will also highlight the physical need for retaining high anisotropy in the heat flux. To characterize the test results, we consider units where the length scale is the domain size L and the time scale is based on the perpendicular thermal diffusivity, $\tau_r = L^2/\chi_\perp$. For constant transport coefficients, the heat transport equation (Eq. 1) becomes,

$$\frac{\partial T}{\partial \hat{t}} - \frac{\chi_\parallel}{\chi_\perp} \hat{\nabla}_\parallel^2 T - \hat{\nabla}_\perp^2 T = S. \quad (9)$$

After temporal discretization, two key parameters characterize the numerical challenges in Eq. 9. The first one is $\Delta \hat{t} \chi_\parallel / \chi_\perp = \Delta t \chi_\parallel / L^2$, which is independent of χ_\perp . The second one is a dimensionless measure of the anisotropy, which can be defined as:

$$\epsilon = \frac{\hat{\tau}_\parallel}{\hat{\tau}_\perp}, \quad (10)$$

where $\hat{\tau}_\parallel$, $\hat{\tau}_\perp$ are fast and slow timescales for the parallel and perpendicular diffusivities, respectively, and are given as [21]:

$$\hat{\tau}_\parallel = \frac{\tau_\parallel}{\tau_r} = \frac{L_\parallel^2}{\chi_\parallel} \frac{\chi_\perp}{L^2} = \frac{\chi_\perp}{\chi_\parallel} \hat{L}_\parallel^2, \quad (11)$$

$$\hat{\tau}_\perp = \frac{\tau_\perp}{\tau_r} = \frac{L_\perp^2}{\chi_\perp} \frac{\chi_\perp}{L^2} = \hat{L}_\perp^2. \quad (12)$$

Here, L_\parallel , L_\perp are parallel and perpendicular temperature-gradient length scales, respectively. Both $\chi_\parallel \Delta t$ and ϵ will be useful to characterize the numerical results below.

3.1. NIMROD benchmark test

The NIMROD benchmark test [8] will allow us to evaluate the numerical pollution for both second- and fourth-order schemes, and verify that they possess the expected scalings as the grid resolution is increased. The comparison between the methods will demonstrate the significant improvement in numerical pollution with the fourth-order method. In addition, the NIMROD benchmark test will allow us to evaluate the performance of the solver as the anisotropy of the heat flux is increased.

The two-dimensional NIMROD test has a heat source $S(x, y) = -\nabla^2 \psi(x, y)$ and a magnetic field $\mathbf{B} = \mathbf{z} \times \nabla \psi$, where the flux function is initialized as $\psi(x, y) = \cos(\pi x) \cos(\pi y)$ in the domain $(x, y) \in (-0.5, 0.5) \times (-0.5, 0.5)$. The temperature has homogeneous Dirichlet boundary conditions at all boundaries. The flux function is time-independent, and therefore the magnetic field is fixed in time. Since ψ is an eigenmode of the Laplacian for the domain and boundary conditions chosen, the temperature remains a flux function at all times and therefore should remain in the null space for the ∇_\parallel operator, $\mathcal{N}(\nabla_\parallel)$. The temperature analytical solution is:

$$T(x, y, t) = \frac{1 - \exp(-2\chi_\perp \pi^2 t)}{\chi_\perp} \psi(x, y), \quad (13)$$

with $T(0, 0, t \rightarrow \infty) = 1/\chi_\perp$.

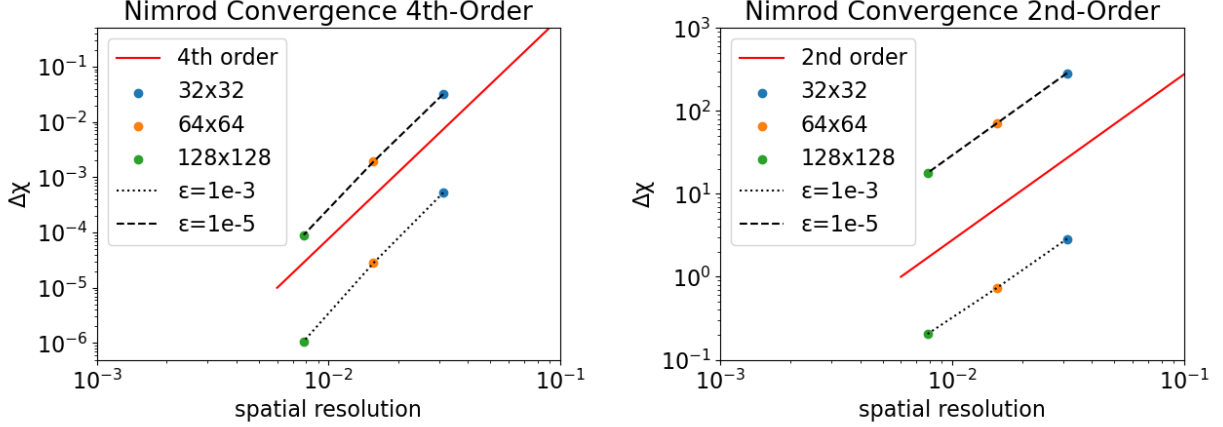


Figure 2: NIMROD benchmark test: relative error $\Delta\chi$ at steady state for second-order and fourth-order discretizations with various grid resolutions and $\epsilon = 10^{-3}, 10^{-5}$. Expected asymptotic convergence rates are recovered by the scheme.

Following [8], a convenient measure of perpendicular numerical pollution is:

$$\Delta\chi = \frac{1}{T(0,0,t \rightarrow \infty)} - \chi_{\perp}, \quad (14)$$

where χ_{\perp} is an input parameter and $T(0,0,t \rightarrow \infty)$ is computed numerically. By design, both parallel and perpendicular length scales are of $\mathcal{O}(1)$, so the anisotropy parameter is simply the ratio of diffusivity coefficients (which are constant in this test), $\epsilon = \chi_{\perp}/\chi_{\parallel}$. This test considers various ϵ -values for both second- and fourth-order schemes at uniform grid resolutions of 32×32 , 64×64 and 128×128 .

We consider accuracy first. Fig. 2 shows that the grid convergence rates for both second- and fourth-order discretizations scale as expected. The numerical pollution can be seen to be greatly reduced by the fourth-order scheme compared to the second-order one, by up to five orders of magnitude. For the second-order method, $\Delta\chi \gg 1$, which makes it unusable in practice as a solver (but performs well as a preconditioner, as we shall see). Finally, Fig. 3 shows that the numerical pollution error scales as $1/\epsilon$ (i.e., the method is not asymptotic-preserving). This is expected behavior whenever the discretization does not have a mesh point exactly at the O-point [12] (which is the case here), since the source of the numerical error is the $\frac{1}{\epsilon} \nabla_{\parallel}^2 T$ term. The magnitude of the error is manageable for the ϵ -values considered owing to the fourth-order accuracy of the scheme.

In regards to performance, Fig. 4-a depicts the results of a grid-convergence study as a function of ϵ for $\Delta t \chi_{\parallel} = 1$. Performance is measured as the average number of GMRES iterations per time step for a relative JFNK nonlinear tolerance of $\epsilon_r = 10^{-3}$. The results demonstrate that the fourth-order method can handle very large anisotropies with minor performance degradation under mesh refinement (an increase of $16 \times$ in the total number of mesh points only results in a $1.5 \times$ increase in GMRES iterations). Also, performance of the solver is independent of ϵ for sufficiently small values. Fig. 4-b shows performance sensitivity with timestep for various ϵ , suggesting that the average number of GMRES iterations per timestep scales as $\sim \sqrt{\Delta t \chi_{\parallel}}$. This scaling favors the use of larger timesteps for efficiency (as

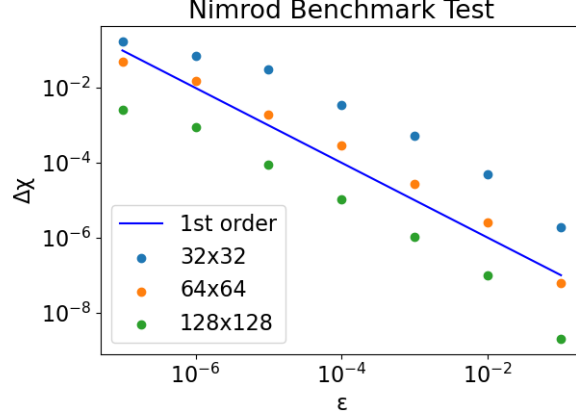


Figure 3: NIMROD benchmark test: scaling of $\Delta\chi$ with the anisotropy ϵ .

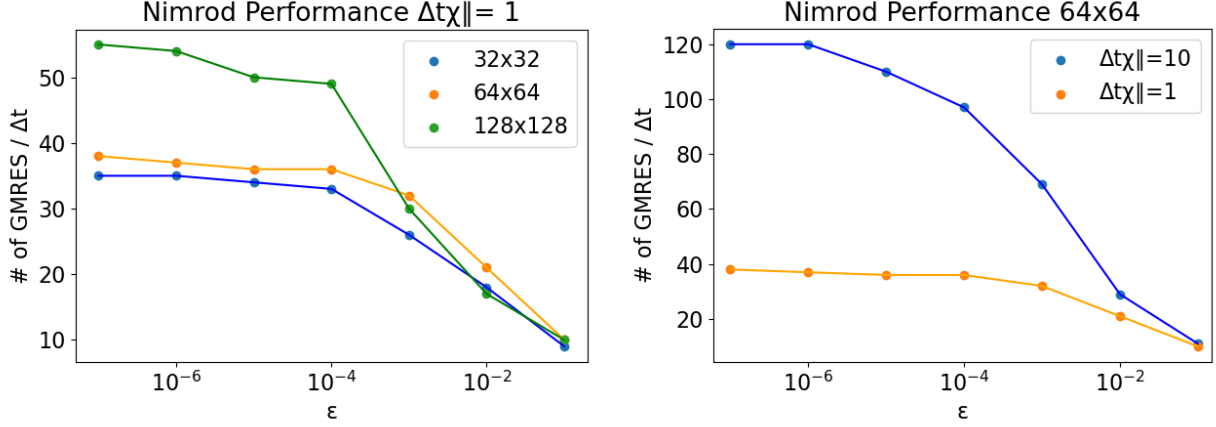


Figure 4: NIMROD benchmark test: number of GMRES iterations per time step vs. ϵ for the fourth-order scheme for (a) different mesh resolutions for $\Delta t\chi_{||} = 1$, and (b) various $\Delta t\chi_{||}$ for the 64×64 mesh.

allowed by the dynamics of interest), since the overall simulation cost scales as $\sim N_{\Delta t} \sqrt{\Delta t} = (t_{final}/\Delta t) \times \sqrt{\Delta t} \sim t_{final}/\sqrt{\Delta t}$.

3.2. Magnetic island test

This test is inspired by a fusion-relevant magnetically confined plasma, and was originally proposed in Ref. [22]. It features a more interesting B-field topology in a 2D cylindrical geometry (r, θ) . The magnetic field is defined by the flux function:

$$\psi(r, \theta) = (r - r_s)^2 + \delta r^2 (1 - r^4) \cos(\theta), \quad (15)$$

in the domain $(r, \theta) \in [0, 1] \times [0, 2\pi)$. The island width is $\delta = 0.005$, with the island located at the rational surface $r_s = 0.7$. The magnetic field is given by $\mathbf{B} = \mathbf{z} \times \nabla\psi + B_z \mathbf{z}$ with a guide field $B_z = 1$, which is much stronger than the poloidal field at the location of the island. As in the NIMROD test, the magnetic field is constant in time.

A time-independent heat source $S(x, y) = 4(1 - r^2)^8$ is prescribed. The initial condition is $T(\mathbf{x}, t = 0) = 0$. Temperature boundary conditions are homogeneous Dirichlet at $r = 1$

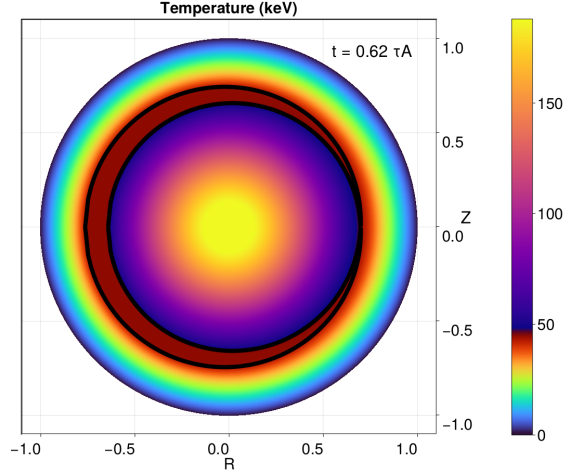


Figure 5: Magnetic island test: steady-state solution ($t = 0.62$) in Cartesian coordinates for $\chi_{\perp}/\chi_{\parallel} = 10^{-7}$ on a 512×256 mesh. The magnetic island separatrix is indicated with a black line.

and regularity at $r = 0$. Since the initial temperature is zero, this test is useful to assess robustness against the development of negative temperatures. The steady-state temperature is reached at $t = 0.62$, and is depicted in Fig. 5. This simulation employed $\Delta t = 10^{-4}$, $\chi_{\parallel} = 10^7$ and $\chi_{\perp} = 1$ (both uniform) on a 512×256 mesh. The flattening of the temperature field within the island is apparent.

Fig. 6 shows radial temperature profiles across the island for various anisotropies, both at early and late times. At early times, the large anisotropy case ($\chi_{\parallel} = 10^7$) retains the flatness of the temperature profile within the island, but this feature is progressively lost as the anisotropy is reduced. The same is true at late times, but the accumulated heat-flux restriction in the high-anisotropy case leads to a substantial decrease in the final temperature at the core. This result highlights the benefits of using as realistic an anisotropy ratio as the discretization allows to capture physical temperature profiles.

The magnetic island test is particularly challenging from a solver-performance standpoint. We measure solver performance for a (very large) timestep $\chi_{\parallel} \Delta t = 10^3$ in terms of the average number of iterations per time step (over the whole simulation until steady state) to achieve a relative tolerance of 5×10^{-3} or a solution update tolerance of $\epsilon_s = 10^{-9}$ (Eq. 7), whichever comes first. First, we consider a grid-convergence study with $\chi_{\parallel}/\chi_{\perp} = 10^7$, with results plotted in Fig. 7-left. The results show no clear dependence of solver performance on the mesh resolution, demonstrating that our second-order MG preconditioner is effective in controlling the iteration count and in rendering the solver almost optimal. The dependence of solver performance on ϵ (with fixed mesh resolution of 512×256) is depicted in Fig. 7-right. The iteration count plateaus at high anisotropy, just as for the NIMROD test in Fig. 4, and the results are consistent with a $\sqrt{\Delta t \chi_{\parallel}}$ scaling for small enough ϵ .

3.3. Bennett screw-pinch kink instability MHD simulation in 2D helical geometry

The third and fourth tests showcase the performance of the scheme in a dynamic magnetohydrodynamics (MHD) simulation using the PIXIE3D MHD code [47, 42]. In this

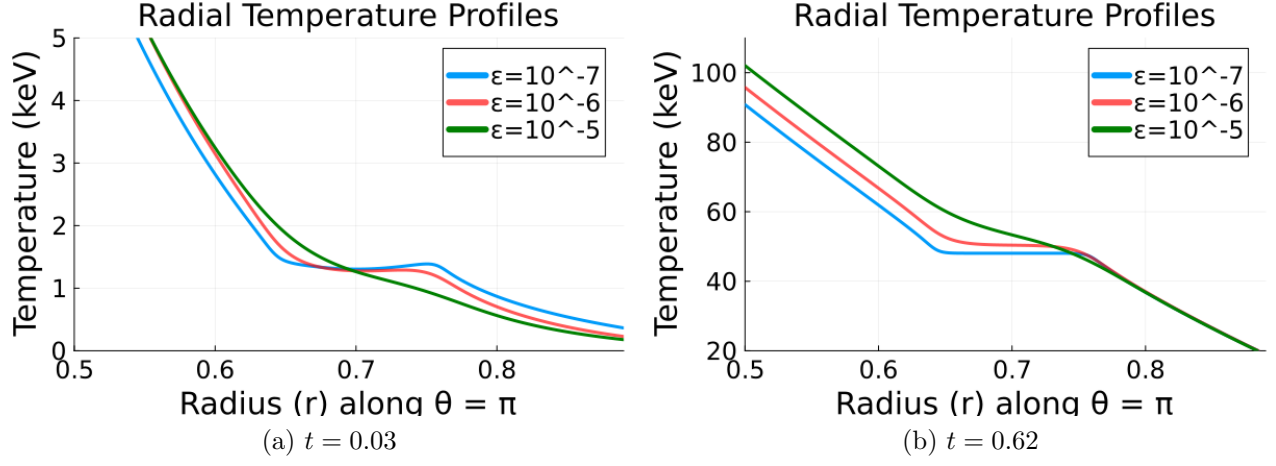


Figure 6: Magnetic island test: temperature profiles across the island at early and late times. At large anisotropy, the flatness of the temperature profile is preserved, whereas lower anisotropies have enough cross-field diffusion to obscure the island's impact on the temperature profile.

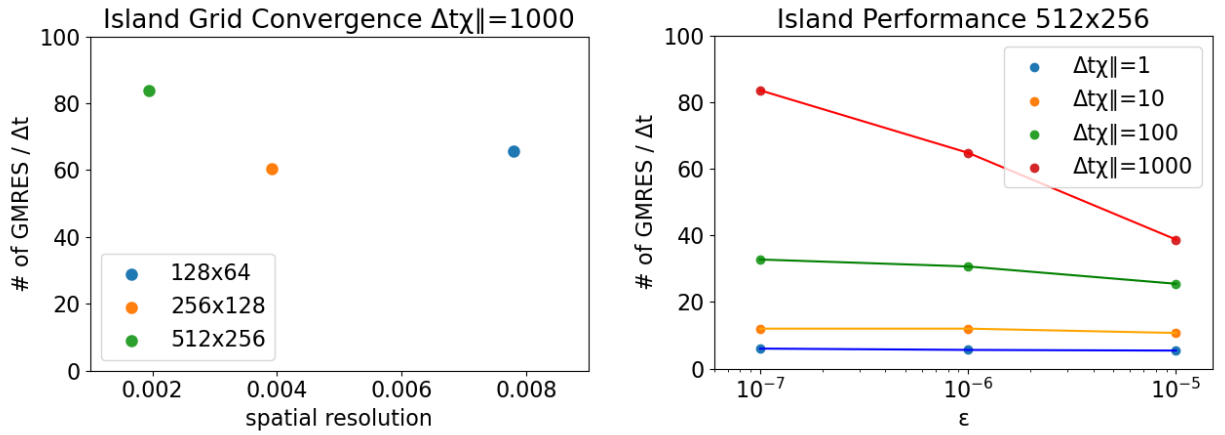


Figure 7: Magnetic island test. Left: Average number of GMRES iterations per time step for various grid resolutions for the island test with $\chi_{||} = 10^7$ and a time step $\Delta t = 10^3/\chi_{||} = 10^{-4}$ showing no clear iteration growth with mesh refinement. Right: Average number of GMRES iterations vs anisotropy $\epsilon \sim \chi_{\perp}/\chi_{||}$ for a 512x256 mesh and various $\Delta t \chi_{||}$ values.

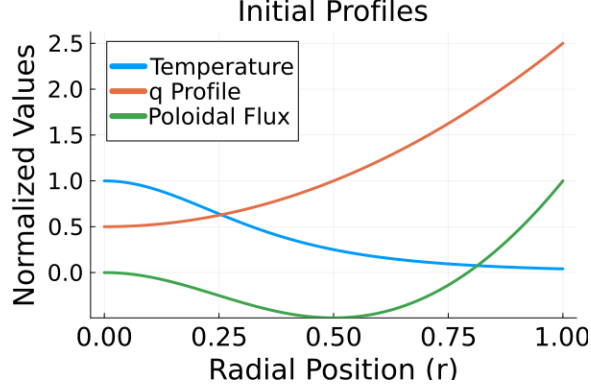


Figure 8: Bennett pinch test: Radial profiles of equilibrium temperature, magnetic flux, and safety factor. The temperature and magnetic flux are normalized to their maximum values.

test, we initialize the simulation with a Bennett pinch equilibrium in cylindrical geometry [35], which only depends on the radial coordinate. The temperature is initialized as $T(r, t = 0) = T_0/4(1 + (4r^2))^2$, with plasma beta $\beta = 1$ and a uniform density. The field components are initialized as $B_\theta(r, t = 0) = 2rB_0/(1 + 4r^2)$ and $B_y(r, t = 0) = B_0$. The temperature T , poloidal magnetic flux Ψ , and safety factor $q = rB_z/RB_\theta$ are depicted in Fig. 8. The instability is seeded at the $q = 1$ rational surface, located at $r = 0.5$. This setup is unstable to a kink instability, resulting in a full magnetic topology reorganization via magnetic reconnection. This reconnection event will allow fast parallel heat transport across the newly formed flux surfaces only after the reconnection event. Such a dramatic display is only possible when the code can handle large heat-transport anisotropies correctly, or else perpendicular numerical pollution will allow the energy to leak across flux surfaces instead of flowing along them.

For the simulation, we consider a non-orthogonal 2D helical projection of the 3D cylinder with domain $(r, \theta) \in [0, 1] \times [0, 2\pi)$ and helical pitch $m/n = 1$, with m, n the mode numbers in the poloidal and axial directions. Boundary conditions are as follows: regularity at $r = 0$ for all quantities; at $r = 1$ we have ideal wall for the magnetic field, homogeneous Neumann for the temperature, and zero-flow for all velocity components; and periodic boundary conditions in θ . Further details of the MHD equations, the 2D helical geometry definition, and the boundary conditions can be found in Ref. [47] (with an update on the treatment of regularity conditions at $r = 0$ in the Appendix of Ref. [48]). We consider realistic functional dependencies for resistivity (Spitzer) and heat-transport coefficients (Braginskii) [1] with temperature T and density ρ , given in Alfvénic dimensionless units as:

$$\eta = \eta_0 \left(\frac{T_{e0}}{T_e} \right)^{\frac{3}{2}}, \quad \chi_\perp = \chi_{\perp 0} \sqrt{\frac{T_{e0}}{T_e} \frac{\rho^2 B_0^2}{\rho_0^2 B^2}}, \quad \chi_\parallel = \chi_{\parallel 0} \left(\frac{T_e}{T_{e0}} \right)^{\frac{5}{2}}.$$

Here, T_{e0} , ρ_0 and B_0 are the reference temperature, density and magnetic-field magnitude, respectively. The dimensionless reference constants are given by $\eta_0 = 5 \times 10^{-4}$, $\chi_{\perp,0} = 5 \times 10^{-4}$ and $\chi_{\parallel,0} = 10^3$. The maximum heat-transport anisotropy ratio is $\chi_{\parallel,0}/\chi_{\perp,0} = 2 \times 10^6$. We also employ a constant ion viscosity $\nu_0 = 5 \times 10^{-4}$ in the momentum equation, and a constant particle diffusivity $D_0 = 5 \times 10^{-4}$ in the continuity equation to ensure smoothness of the density field around the coordinate singularity. We consider a 128×64 mesh. We employ

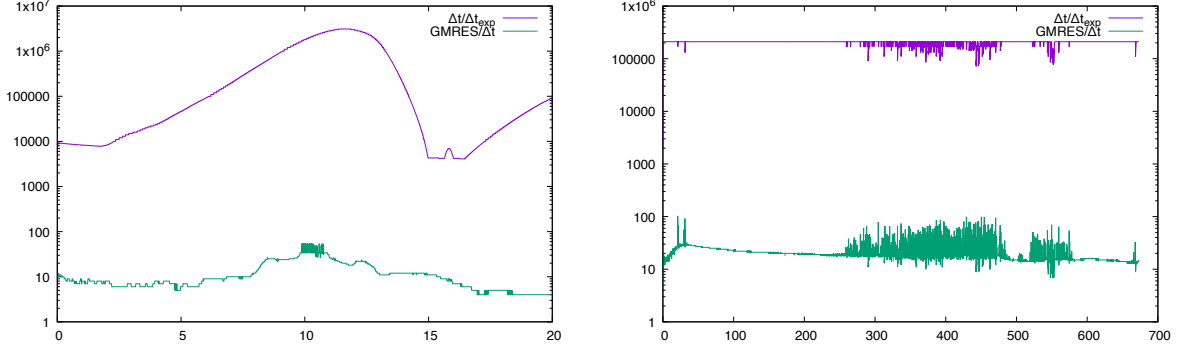


Figure 9: Time history of the $\Delta t/\Delta t_{exp}$ ratio and the number of GMRES iterations per timestep for the Bennett test (left), and the ITER test (right).

an implicit timestep of $\Delta t = 10^{-2}\tau_A$ (with $\tau_A = L/v_A$ the Alfvén time, and $v_A = B_0/\sqrt{\rho_0\mu_0}$ the Alfvén speed). This timestep corresponds to $\Delta t\chi_{\parallel} = 10$. The equilibrium is perturbed at $t = 0$ with a small radial velocity, $V_r(r, \theta, t = 0) = 10^{-3} \sin(\pi r) \cos \theta$.

At the beginning of the simulation, the implicit timestep is about $9300\times$ larger than the explicit stability limit, Δt_{exp} , and peaks at $\sim 3.1 \times 10^6 \Delta t_{exp}$ during the simulation. We run the simulation until $t = 20\tau_A$. For this test, the relative JFNK tolerance is $\epsilon_r = 10^{-3}$, and we use V(5,5) MG V-cycles for all the MG solves in the MHD preconditioner, including the transport equation [42]. The average number of GMRES iterations per timestep over the whole simulation for the 128×64 mesh resolution is 12.0. The iteration and $\Delta t/\Delta t_{exp}$ histories are provided in Fig. 9-left, demonstrating excellent algorithmic performance of the MHD solver with the strongly anisotropic transport physics throughout the simulation despite the very large implicit timestep used.

Snapshots of the temperature profiles overlayed with the flux surfaces are shown in Fig. 10. The fast reconnection event occurs around $t = 16.1$. Before the event, most of the thermal energy is contained within the flux surfaces near the X-point. Quickly after the reconnection event, this energy can be seen to rapidly spread along the flux surfaces and fill the volume. The sharpness of the results in this MHD simulation demonstrates the ability of the scheme to perform accurately in highly coupled, nonlinear MHD simulations on non-trivial geometries including coordinate singularities (at $r = 0$) and non-orthogonal geometries (helical).

3.4. ITER kink instability MHD simulation in 3D toroidal geometry

For our last test, we consider a fully 3D ITER tokamak MHD simulation of an unstable equilibrium in realistic non-orthogonal toroidal geometry. The equilibrium is unstable to a $m = 1, n = 1$ internal kink mode. The initial pressure and safety-factor profiles are shown in Fig. 11-left; the poloidal flux is provided in Fig. 11-right. Spitzer resistivity and Braginskii heat-transport coefficients are used as in the previous test, with $\eta_0 = 10^{-4}$, $\chi_{\perp,0} = 2 \times 10^{-6}$, $\chi_{\parallel,0} = 20.0$ (seven orders of magnitude in thermal transport anisotropy). Additionally, we use $D_0 = 5 \times 10^{-4}$ and $\nu_0 = 10^{-4}|1 + 4.6r^3|^4$, where r is the radial logical coordinate. The logical-to-physical coordinate map used for this simulation is described in Appendix B. The increased viscosity at the edge of the plasma prevents generation of spurious oscillations in

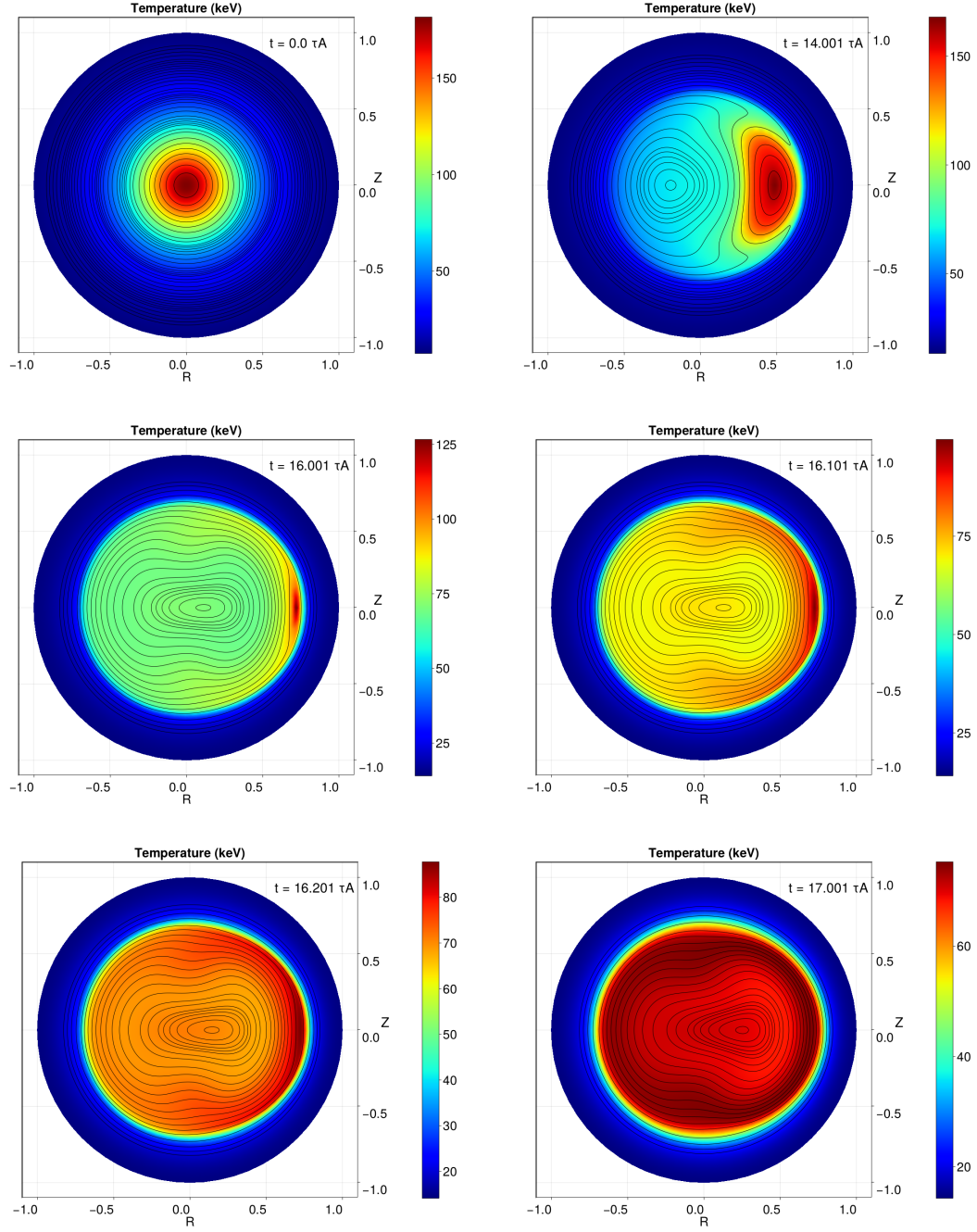


Figure 10: Bennett pinch test: Temperature snapshots of the closed flux surfaces for the helical test at a resolution of 128×64 . Timestamps provided in the figures. Note that the color bar rescales with the maximum temperature at each snapshot.

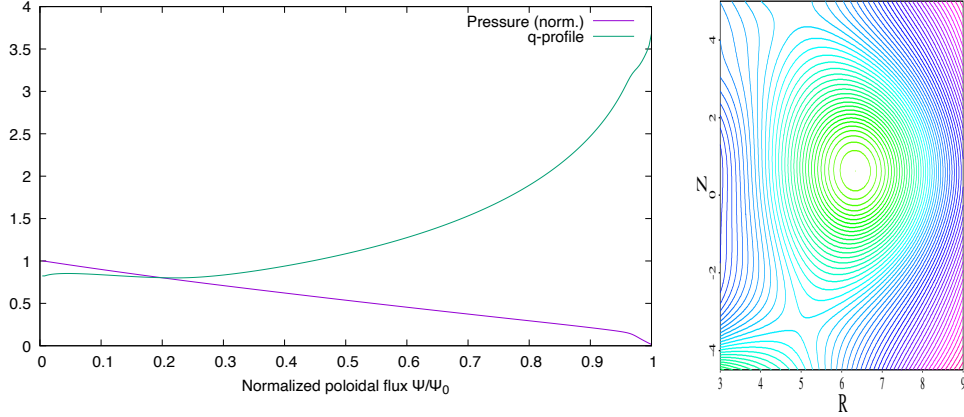


Figure 11: ITER test. Left: Profiles of initial pressure, and q-profile as a function of the poloidal flux, normalized to the separatrix flux value. The pressure is normalized to the plasma beta, $\beta = 0.028$. Right: ITER equilibrium poloidal flux.

the cold plasma near the wall. With seven orders of magnitude of transport anisotropy, thermal energy rapidly equalizes along field lines with very little diffusion across them.

The simulation employs a timestep $\Delta t = 0.1\tau_A$ (which corresponds to $\Delta t\chi_{\parallel} = 2$) and a uniform logical grid resolution of $128 \times 64 \times 32$, partitioned into 512 parallel domains. The simulation is initialized with a small applied radial velocity perturbation, $V_r(r, \theta, t = 0) = 10^{-4} \sin(\pi r) \cos(\theta)$, where r here is the logical radial coordinate and θ the logical poloidal-angle coordinate. The number of GMRES iterations needed per timestep to achieve a relative residual of 10^{-3} is 25.5, averaged over the entire simulation duration of 16,277 timesteps. The iteration and $\Delta t/\Delta t_{exp}$ histories are provided in Fig. 9-right, with similar conclusions as with the Bennett test.

The evolving magnetic topology and temperature field during the ensuing disruption are shown via Poincare sections and temperature plots in Figure 12, respectively. As the (1,1) kink mode develops, the thermal energy of the core is seen to remain within the region of closed flux surfaces, as expected. This result highlights the suitability of our method for realistic 3D MHD applications in realistic geometries and highly dynamic scenarios.

4. Conclusions

We have demonstrated a practical high-order scheme for the strongly anisotropic heat transport equation that is easy to implement in existing finite-difference implementations, is fourth-order accurate, is robust, and offers manageable numerical errors for realistically large anisotropies (with up to 10^7 considered in this study). Critically, the approach is amenable to modern multigrid solvers for implicit time integration, rendering the implementation scalable under grid refinement (i.e., with the number of GMRES iterations per timestep very weakly dependent on the number of mesh points and transport anisotropy), and scaling as $\sqrt{\Delta t\chi_{\parallel}}$ with the implicit timestep. The approach has been demonstrated with well-accepted targeted numerical tests, as well as integrated MHD simulations of kink instabilities in magnetically confined tokamak fusion reactors in both idealized (helical) and realistic (toroidal) geometries. We conclude that the method offers a viable, practical and efficient numerical

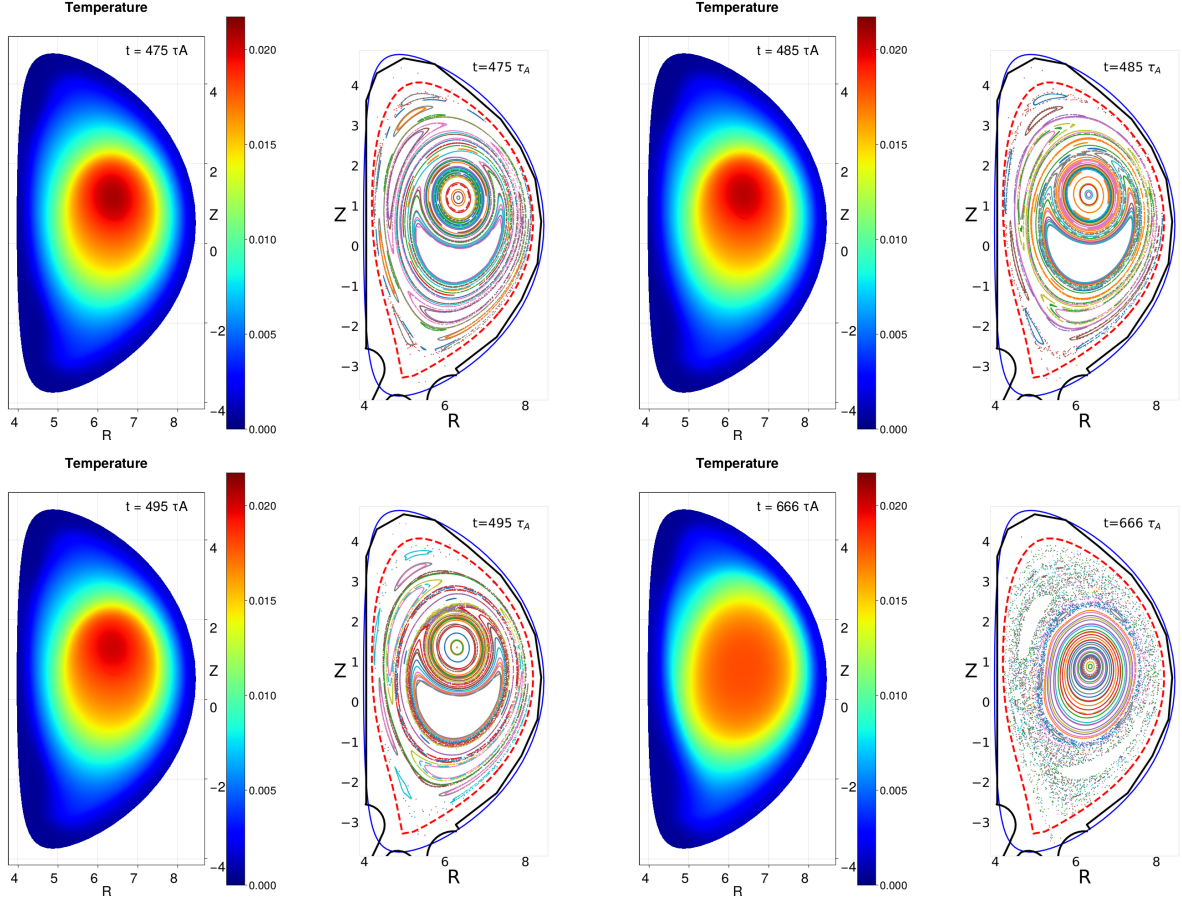


Figure 12: ITER test: Snapshots of the temperature (shown with the color map) and magnetic topology (shown with the Poincaré maps) before, during, and after the reconnection event, with a resolution of $128 \times 64 \times 32$. Timestamps are provided in the figures. The temperature remains confined to the closed flux surfaces.

scheme to deal with the strongly anisotropic transport equation in realistic plasma conditions and geometries.

Acknowledgments

The authors acknowledge useful conversations with X. Tang and J. N. Shadid. This work was supported by Triad National Security, LLC under contract 89233218CNA000001, and the DOE Office of Applied Scientific Computing Research (ASCR) through the DOE FES-ASCR SciDAC Partnership Program and the ASCR Applied Mathematics Program. The research used computing resources provided by the Los Alamos National Laboratory Institutional Computing Program.

Appendix A. Implementation details of the fourth-order accurate discretization

The full discrete treatment of the anisotropic tensor-diffusion operator for both inner-domain and boundary points is as follows. We begin with a conservative divergence discretization in 2D (with straightforward generalization to 3D):

$$\begin{aligned} \nabla \cdot (\bar{\Xi} \cdot \nabla \varphi) |_{i,j} &= \frac{1}{\Delta x} \left[\left(\Xi^{xx} \frac{\partial \varphi}{\partial x} + \Xi^{xy} \frac{\partial \varphi}{\partial y} \right)_{i+1/2,j} - \left(\Xi^{xx} \frac{\partial \varphi}{\partial x} + \Xi^{xy} \frac{\partial \varphi}{\partial y} \right)_{i-1/2,j} \right] \\ &+ \frac{1}{\Delta y} \left[\left(\Xi^{yy} \frac{\partial \varphi}{\partial y} + \Xi^{xy} \frac{\partial \varphi}{\partial x} \right)_{i,j+1/2} - \left(\Xi^{yy} \frac{\partial \varphi}{\partial y} + \Xi^{xy} \frac{\partial \varphi}{\partial x} \right)_{i,j-1/2} \right]. \end{aligned}$$

For the co-derivative fluxes at faces, we interpolate the face-centered flux from cell-centered values of φ to fourth-order accuracy as follows:

$$\left(\Xi^{xx} \frac{\partial \varphi}{\partial x} \right)_{i+1/2,j} = \frac{1}{\Delta x} \begin{cases} C_{1 \times 5}^+ \Xi_{N_x-3:N_x+1,j}^{xx} A_{2:6,6} \varphi_{N_x-4:N_x+1,j}, & i = N_x \\ C_{1 \times 4}^0 \Xi_{N_x-2:N_x+1,j}^{xx} A_{3:6,6} \varphi_{N_x-4:N_x+1,j}, & i = N_x - 1 \\ C_{1 \times 4}^0 \Xi_{i-1:i+2,j}^{xx} A_{2:5,6} \varphi_{i-2:i+3,j}, & 2 \leq i \leq N_x - 2, \\ C_{1 \times 4}^0 \Xi_{0:3,j}^{xx} A_{1:4,6} \varphi_{0:5,j}, & i = 1 \\ C_{1 \times 5}^- \Xi_{0:4,j}^{xx} A_{1:5,6} \varphi_{0:5,j}, & i = 0 \end{cases}$$

and similarly for $\left(\Xi^{yy} \frac{\partial \varphi}{\partial y} \right)_{i,j+1/2}$, with:

$$\begin{aligned} C_{1 \times 4}^0 &= \frac{1}{12} (-1, 7, 7, -1), \\ C_{1 \times 5}^+ &= \frac{1}{12} (2, 17, -11, 5, -1), \\ C_{1 \times 5}^- &= \frac{1}{12} (-1, 5, -11, 17, 2), \end{aligned}$$

and:

$$A_{6 \times 6} = \frac{1}{60} \begin{pmatrix} -137 & 300 & -300 & 200 & -75 & 12 \\ -12 & -65 & 120 & -60 & 20 & -3 \\ 3 & -30 & -20 & 60 & -15 & 2 \\ -2 & 15 & -60 & 20 & 30 & -3 \\ 3 & -20 & 60 & -120 & 65 & 12 \\ -12 & 75 & -200 & 300 & -300 & 137 \end{pmatrix}.$$

For the cross-derivative fluxes, a similar fourth-order interpolation yields:

$$\left(\Xi^{xy} \frac{\partial \varphi}{\partial y} \right)_{i+1/2,j} = \begin{cases} C_{1 \times 5}^+ \left(\Xi^{xy} \frac{\partial \varphi}{\partial y} \right)_{N_x-3:N_x+1,j}, & i = N_x \\ C_{1 \times 4}^0 \left(\Xi^{xy} \frac{\partial \varphi}{\partial y} \right)_{i-1:i+2,j}, & 1 \leq i < N_x - 1, \\ C_{1 \times 5}^- \left(\Xi^{xy} \frac{\partial \varphi}{\partial y} \right)_{0:4,j}, & i = 0 \end{cases}$$

with:

$$\left(\Xi^{xy} \frac{\partial \varphi}{\partial y} \right)_{i,j} = \frac{\Xi_{i,j}^{xy}}{\Delta y} \begin{cases} D_{1 \times 5}^0 \varphi_{i,j-2:j+2}^T, & 2 \leq j \leq N_y - 1 \\ D_{1 \times 5}^- \varphi_{i,0:5}^T, & j = 0, 1 \\ D_{1 \times 5}^+ \varphi_{i,N_y-3:N_y+1}^T, & j = N_y, N_y + 1 \end{cases},$$

and:

$$\begin{aligned} D_{1 \times 5}^0 &= \frac{1}{12}(1, -8, 0, 8, -1), \\ D_{1 \times 5}^+ &= \frac{1}{12}(-1, 6, -18, 10, 3), \\ D_{1 \times 5}^- &= \frac{1}{12}(-3, -10, 18, -6, 1). \end{aligned}$$

Appendix B. Logical-to-physical coordinate map in the ITER simulation

The ITER kink mode simulation of Section 3.4 uses a logical coordinate system $(r, \theta, \phi) \in [0, 1] \times [0, 2\pi) \times [0, 2\pi)$. The logical coordinates are mapped to cylindrical coordinates using the transformation:

$$\begin{aligned} R(r, \theta, \phi) &= R_m + (R_0 - R_m)r + ar \cos[\theta + \arcsin(\delta r^2 \sin \theta)], \\ Z(r, \theta, \phi) &= Z_m + (Z_0 - Z_m)r + a(r\kappa + (1-r)\kappa_s)r \sin[\theta + \zeta r^2 \sin(2\theta)], \\ \phi_c(\phi) &= -\phi. \end{aligned}$$

The shaping parameters for the ITER experiment are: minor radius $a = 2.24\text{m}$, geometric axis $R_0 = 6.219577546\text{m}$, $Z_0 = 0.5143555944\text{m}$, magnetic axis $R_m = 6.341952203\text{m}$, $Z_m = 0.6327986088\text{m}$, triangularity $\delta = 0.6$, elongation $\kappa = 1.9$, elongation at the magnetic axis $\kappa_s = 1.35$, and squareness $\zeta = 0.06$. We emphasize that the cylindrical angle ϕ_c rotates about the origin in the opposite direction as the toroidal angle ϕ .

References

- [1] S. I. Braginskii, “Transport processes in a plasma,” in *Reviews of Plasma Physics* (M. A. Leontovich, ed.), vol. 1, pp. 205–311, New York: Consultants Bureau, 1965.
- [2] M. Hölzl, S. Günter, I. Classen, Q. Yu, E. Delabie, T. Team, *et al.*, “Determination of the heat diffusion anisotropy by comparing measured and simulated electron temperature profiles across magnetic islands,” *Nuclear fusion*, vol. 49, no. 11, p. 115009, 2009.
- [3] C. Ren, J. D. Callen, T. A. Gianakon, C. C. Hegna, Z. Chang, E. D. Fredrickson, K. M. McGuire, G. Taylor, and M. C. Zarnstorff, “Measuring Δ' from electron temperature fluctuations in the Tokamak Fusion Test Reactor,” *Physics of Plasmas*, vol. 5, no. 2, pp. 450–454, 1998.
- [4] J. Meskat, H. Zohm, G. Gantenbein, S. Günter, M. Maraschek, W. Suttrop, Q. Yu, and A. U. Team, “Analysis of the structure of neoclassical tearing modes in ASDEX Upgrade,” *Plasma Physics and Controlled Fusion*, vol. 43, no. 10, p. 1325, 2001.
- [5] J. Snape, K. Gibson, T. O’gorman, N. Barratt, K. Imada, H. Wilson, G. Tallents, I. Chapman, *et al.*, “The influence of finite radial transport on the structure and evolution of $m/n=2/1$ neoclassical tearing modes on MAST,” *Plasma Physics and Controlled Fusion*, vol. 54, no. 8, p. 085001, 2012.
- [6] M. J. Choi, G. S. Yun, W. Lee, H. K. Park, Y.-S. Park, S. A. Sabbagh, K. J. Gibson, C. Bowman, C. W. Domier, N. C. Luhmann Jr, *et al.*, “Improved accuracy in the estimation of the tearing mode stability parameters (Δ' and ω_c) using 2D ECEI data in KSTAR,” *Nuclear Fusion*, vol. 54, no. 8, p. 083010, 2014.
- [7] M. Umansky, M. Day, and T. Rognlien, “On numerical solution of strongly anisotropic diffusion equation on misaligned grids,” *Numerical Heat Transfer, Part B: Fundamentals*, vol. 47, no. 6, pp. 533–554, 2005.
- [8] C. Sovinec, A. Glasser, T. Gianakon, D. Barnes, R. Nebel, S. Kruger, D. Schnack, S. Plimpton, A. Tarditi, M. Chu, *et al.*, “Nonlinear magnetohydrodynamics simulation using high-order finite elements,” *Journal of Computational Physics*, vol. 195, no. 1, pp. 355–386, 2004.
- [9] S. Günter, K. Lackner, and C. Tichmann, “Finite element and higher order difference formulations for modelling heat transport in magnetised plasmas,” *Journal of Computational Physics*, vol. 226, no. 2, pp. 2306–2316, 2007.
- [10] S. Günter, Q. Yu, J. Krüger, and K. Lackner, “Modelling of heat transport in magnetised plasmas using non-aligned coordinates,” *Journal of Computational Physics*, vol. 209, no. 1, pp. 354–370, 2005.
- [11] B. van Es, B. Koren, and H. J. de Blank, “Finite-difference schemes for anisotropic diffusion,” *Journal of Computational Physics*, vol. 272, pp. 526–549, 2014.

- [12] B. van Es, B. Koren, and H. J. de Blank, “Finite-volume scheme for anisotropic diffusion,” *Journal of Computational Physics*, vol. 306, pp. 422–442, 2016.
- [13] P. Sharma and G. W. Hammett, “Preserving monotonicity in anisotropic diffusion,” *J. Comput. Phys.*, vol. 227, pp. 123–142, NOV 10 2007.
- [14] C. Le Potier, “Finite volume scheme satisfying maximum and minimum principles for anisotropic diffusion operators,” *Finite volumes for complex applications V*, pp. 103–118, 2008.
- [15] D. Kuzmin, M. J. Shashkov, and D. Svyatskiy, “A constrained finite element method satisfying the discrete maximum principle for anisotropic diffusion problems,” *J. Comput. Phys.*, vol. 228, pp. 3448–3463, MAY 20 2009.
- [16] K. Lipnikov, D. Svyatskiy, and Y. Vassilevski, “Minimal stencil finite volume scheme with the discrete maximum principle,” *Russian Journal of Numerical Analysis and Mathematical Modelling*, vol. 27, no. 4, pp. 369–386, 2012.
- [17] E. J. Du Toit, M. R. O’Brien, and R. G. Vann, “Positivity-preserving scheme for two-dimensional advection–diffusion equations including mixed derivatives,” *Computer Physics Communications*, vol. 228, pp. 61–68, 2018.
- [18] D. Thangaraj and A. Nathan, “A rotated monotone difference scheme for the two-dimensional anisotropic drift-diffusion equation,” *Journal of Computational Physics*, vol. 145, no. 1, pp. 445–461, 1998.
- [19] C. Le Potier, “Un schéma linéaire vérifiant le principe du maximum pour des opérateurs de diffusion très anisotropes sur des maillages déformés,” *Comptes Rendus Mathématique*, vol. 347, no. 1-2, pp. 105–110, 2009.
- [20] C. Ngo and W. Huang, “Monotone finite difference schemes for anisotropic diffusion problems via nonnegative directional splittings,” *Communications in Computational Physics*, vol. 19, no. 2, pp. 473–495, 2016.
- [21] L. Chacón, D. del Castillo-Negrete, and C. D. Hauck, “An asymptotic-preserving semi-lagrangian algorithm for the time-dependent anisotropic heat transport equation,” *Journal of Computational Physics*, vol. 272, pp. 719–746, 2014.
- [22] S. Günter and K. Lackner, “A mixed implicit–explicit finite difference scheme for heat transport in magnetised plasmas,” *Journal of Computational Physics*, vol. 228, no. 2, pp. 282–293, 2009.
- [23] L. Li and C. Yang, “Block preconditioning methods for asymptotic preserving scheme arising in anisotropic elliptic problems,” *Journal of Scientific Computing*, vol. 99, no. 3, p. 63, 2024.
- [24] P. Degond, A. Lozinski, J. Narski, and C. Negulescu, “An asymptotic-preserving method for highly anisotropic elliptic equations based on a micro–macro decomposition,” *Journal of Computational Physics*, vol. 231, no. 7, pp. 2724–2740, 2012.

- [25] P. Degond, F. Deluzet, A. Lozinski, J. Narski, and C. Negulescu, “Duality-based asymptotic-preserving method for highly anisotropic diffusion equations,” *Communications in Mathematical Sciences*, vol. 10, pp. 1–31, 2012.
- [26] P. Degond, F. Deluzet, and C. Negulescu, “An asymptotic preserving scheme for strongly anisotropic elliptic problems,” *Multiscale Modeling & Simulation*, vol. 8, no. 2, pp. 645–666, 2010.
- [27] J. Narski and M. Ottaviani, “Asymptotic preserving scheme for strongly anisotropic parabolic equations for arbitrary anisotropy direction,” *Computer Physics Communications*, vol. 185, no. 12, pp. 3189–3203, 2014.
- [28] Y. Wang, W. Ying, and M. Tang, “Uniformly convergent scheme for strongly anisotropic diffusion equations with closed field lines,” *SIAM Journal on Scientific Computing*, vol. 40, no. 5, pp. B1253–B1276, 2018.
- [29] D. del Castillo-Negrete and L. Chacón, “Local and nonlocal parallel heat transport in general magnetic fields,” *Physical review letters*, vol. 106, no. 19, p. 195004, 2011.
- [30] D. del Castillo-Negrete and L. Chacón, “Parallel heat transport in integrable and chaotic magnetic fields,” *Physics of Plasmas*, vol. 19, no. 5, p. 056112, 2012.
- [31] L. Chacón and G. Di Giannatale, “An asymptotic-preserving semi-lagrangian algorithm for the anisotropic heat transport equation with arbitrary magnetic fields,” *Journal of Computational Physics*, p. 113368, 2024.
- [32] O. Koshkarov and L. Chacón, “A fully implicit, asymptotic-preserving, semi-lagrangian algorithm for the time dependent anisotropic heat transport equation,” *Journal of Computational Physics*, p. 113381, 2024.
- [33] D. A. Knoll and D. E. Keyes, “Jacobian-free Newton-Krylov methods: a survey of approaches and applications.,” *J. Comput. Phys.*, vol. 193, no. 2, pp. 357 – 97, 2004.
- [34] P. H. Gaskell and A. K. C. Lau, “Curvature-compensated convective transport: SMART, a new boundedness-preserving transport algorithm,” *International Journal for Numerical Methods in Fluids*, vol. 8, pp. 617–641, 1988.
- [35] W. H. Bennett, “Magnetically self-focussing streams,” *Physical Review*, vol. 45, no. 12, p. 890, 1934.
- [36] P. Sharma and G. W. Hammett, “Preserving monotonicity in anisotropic diffusion,” *Journal of Computational Physics*, vol. 227, no. 1, pp. 123–142, 2007.
- [37] V. Gyrya and K. Lipnikov, “The arbitrary order mimetic finite difference method for a diffusion equation with a non-symmetric diffusion tensor,” *Journal of Computational Physics*, vol. 348, pp. 549–566, 2017.
- [38] G. D. Byrne and A. C. Hindmarsh, “A polyalgorithm for the numerical solution of ordinary differential equations,” *ACM Transactions on Mathematical Software*, vol. 1, no. 1, pp. 71–96, 1975.

- [39] Y. Saad, “A flexible inner-outer preconditioned GMRES algorithm,” *SIAM J. Sci. Comput.*, vol. 14, no. 2, pp. 461–469, 1992.
- [40] R. Dembo, S. Eisenstat, and R. Steihaug, “Inexact Newton methods,” *J. Numer. Anal.*, vol. 19, p. 400, 1982.
- [41] L. Chacón and D. A. Knoll, “A 2D high- β Hall MHD implicit nonlinear solver,” *J. Comput. Phys.*, vol. 188, no. 2, pp. 573–592, 2003.
- [42] L. Chacón, “An optimal, parallel, fully implicit Newton-Krylov solver for three-dimensional visco-resistive magnetohydrodynamics,” *Phys. Plasmas*, vol. 15, p. 056103, 2008.
- [43] A. Brandt and O. E. Livne, *Multigrid Techniques: 1984 Guide with Applications to Fluid Dynamics, Revised Edition*. SIAM, 2011.
- [44] L. Chacón, “A scalable multidimensional fully implicit solver for hall magnetohydrodynamics,” *arXiv preprint arXiv:2407.07031*, 2024.
- [45] W. L. Briggs, *A Multigrid Tutorial*. Philadelphia, PA: SIAM, 1987.
- [46] P. Wesseling, *An Introduction to Multigrid Methods*. Chichester: John Wiley & Sons, 1992.
- [47] L. Chacón, “A non-staggered, conservative, $\nabla \cdot \mathbf{B} = 0$, finite-volume scheme for 3D implicit extended magnetohydrodynamics in curvilinear geometries,” *Comput. Phys. Commun.*, vol. 163, pp. 143–171, 2004.
- [48] G. L. Delzanno, L. Chacón, and J. M. Finn, “Electrostatic mode associated with the pinch velocity in reversed field pinch simulations,” *Physics of Plasmas*, vol. 15, no. 12, 2008.